Stable All-Solid-State Lithium Metal Batteries Enabled by Machine Learning Simulation Designed Halide Electrolytes

Feng Li,◆ Xiaobin Cheng,◆ Lei-Lei Lu, Yi-Chen Yin, Jin-Da Luo, Gongxun Lu, Yu-Feng Meng, Hongsheng Mo, Te Tian, Jing-Tian Yang, Wen Wen, Zhi-Pan Liu, Guozhen Zhang,* Cheng Shang,* and Hong-Bin Yao*

ACCESS | Metrics & More | Article Recommendations | Supporting Information

ABSTRACT: Solid electrolytes (SEs) with superionic conductivity and interfacial stability are highly desirable for stable all-solid-state Li-metal batteries (ASSLMBs). Here, we employ neural network potential to simulate materials composed of Li, Zr/Hf, and Cl using stochastic surface walking method and identify two potential unique layered halide SEs, named Li_2ZrCl_6 and Li_2HfCl_6, for stable ASSLMBs. The predicted halide SEs possess high Li^+ conductivity and outstanding compatibility with Li metal anodes. We synthesize these SEs and demonstrate their superior stability against Li metal anodes with a record performance of 4000 h of steady lithium plating/stripping. We further fabricate the prototype stable ASSLMBs using these halide SEs without any interfacial modifications, showing small internal cathode/SE resistance (19.48 Ω cm^2), high average Coulombic efficiency (~99.48%), good rate capability (63 mAh g^{-1} at 1.5 C), and unprecedented cycling stability (87% capacity retention for 70 cycles at 0.5 C).

☑ Atomic simulation
☑ Novel Layered-structure
☑ Superionic conductor
☑ Compatibility Vs. Li-metal
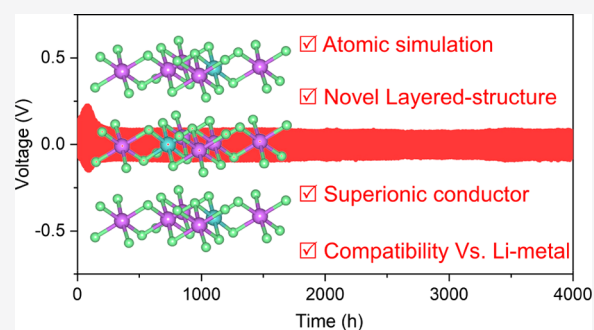
KEYWORDS: neural network, machine learning, layered halide electrolytes, Li metal anode compatibility, all-solid-state batteries

With future global decarbonization, a Li-metal battery possessing high energy density is a promising energy storage system for the electrification of transport and grid-scale accessibility of solar and wind energy.[1,2] Its practical application, however, is severely hampered by the potential safety risks due to the flammability of conventional liquid electrolytes (LEs).[3] This problem is motivating the extensive search for alternative electrolytes to realize a safe and powerful Li-metal battery. Solid electrolytes (SEs) made from a nonflammable inorganic compound have been proposed as a potential replacement of LEs, giving rise to all-solid-state Li-metal batteries (ASSLMBs) to address the safety issues and concurrently achieve the requirement of energy/power density.[4] It is well-known that the central part of developing ASSLMBs is the exploration of SEs possessing high ionic conductivity and excellent interfacial stability.[5]

In the past few decades, tremendous effort has been devoted on the design of advanced SEs. Oxide, sulfide, and halide SEs with high Li^+ conductivity (10^{-4}–10^{-2} S cm^{-1}) have been considered as promising candidates for ASSLMBs.[6−12] However, it remains a great challenge to fabricate stable ASSLMBs directly using these SEs due to the undesirable trade-off between Li^+ conductivity and interfacial stability. Although oxide SEs show good electrochemical stability with electrodes,[6,13−15] the ineffective solid−solid contacts restrain fast transport of Li^+ due to the poor lattice deformability of

oxides.[16] Sulfide SEs have exhibited desirable ductile nature and high Li^+ conductivity.[11] Unfortunately, the incorporation of sulfide SEs in ASSLMBs faces considerable inherent instability toward air/moisture, high-voltage cathodes,[17] and Li-metal (except for $Li_{9.6}P_3S_{12}$, ~0 V vs Li).[11] Recently emerged Li_3MCl_6 (M = Y, Er, In, Sc)[18−22] halide SEs have exhibited compatibility with bare-cathodes (LiCoO$_2$, LCO; LiNi$_{1−x−y}$Mn$_x$Co$_y$O$_2$, NMC),[18,22] but these halide SEs cannot directly couple with Li-metal due to the poor reduction stability of trivalent transition-metal cations.[18,20,22]

An original idea for the design of SEs is first to choose properly primary elements and then to construct soft framework for fast Li^+ conduction and compact solid−solid contacts. In consideration of soft lattices of halide SEs[23] and good interfacial stability of zirconium-based oxide SEs,[8,14,24] it is promising to design stable halide SEs on the basis of primary Li, Zr/Hf, and Cl elements. However, without prior knowledge of the crystal structure there is a need for a tremendous
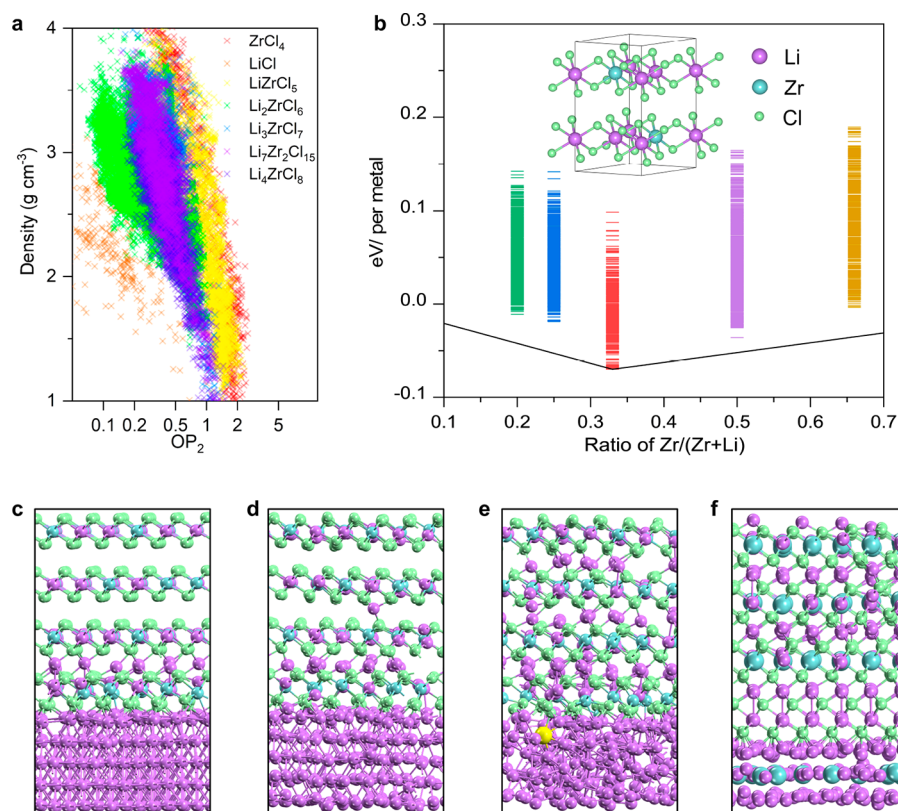
Figure 1. Training data set for the Li−Zr−Cl NN potential training. (a) Plot of all training data set (34 648 in total) for the Li−Zr−Cl NN potential training. The x-axis is a distance-weighted Steinhart order parameter (OP),[36,37] the y-axis is the density of each configuration. The colored points correspond to different x of $(LiCl)_{1-x}(ZrCl_4)_x$. (b) Thermodynamics convex hull diagram for $(LiCl)_{1-x}(ZrCl_4)_x$ phases with respect to the global minimum (GM) of LiCl and $ZrCl_4$ bulk. The energy spectrum from DFT optimized structures for each composition is also shown in the color bar. The inset shows the GM configuration of Li_2ZrCl_6. The crystal structures are visualized using VESTA.[38] (c−f) Four representative structures for Li/LZrC interface correspond to structures at 0, 1, and 35 ps along the MD trajectory at 300 K and an optimized minimum after a 2 ns MD simulation at 400 K, respectively. The Li, Zr, and Cl atoms are represented by purple, cyan, and green spheres, respectively. Note that the yellow ball in (e) denotes the Zr atoms that dissolve into Li metal.

amount work to identify a suitable and stable crystal structure for superior Li$^+$ conduction from scratch only that initially started from primary elements.

The application of artificial intelligence in physical sciences has brought an unprecedented opportunity to expedite a chemical structure search.[25−27] Recently, neural network atomic potentials based on first-principles data can accelerate simulation by up to 3−4 orders of magnitude without significant sacrifice of accuracy compared to first-principles computation, making high throughput screening of tens of thousands of possible structures affordable. The recent developed Stochastic Surface Walking global optimization[28] combined with global Neural Network potential (SSW-NN) method[29,30] is a powerful toolkit holding the great promise for rapid structure prediction and mechanism investigation in catalysis,[31−33] electrodes, and electrolytes.[34,35]

In this work, for the first time we use the SSW-NN method to realize the rational design of halide SEs, showing novel layered structures of Li−Zr/Hf−Cl to achieve superfast Li$^+$ conduction and interfacial stability and demonstrate the feasibility of the first-principles design of SEs. We employ SSW-NN to search out the most stable structure of Li−Zr/Hf−Cl ternary components. According to the structure prediction, we use the mechanochemical method to synthesize the SEs. The obtained Li_2MCl_6 (M = Zr, Hf) has high Li$^+$ conductivity up to ~1 mS cm^{-1}. More importantly, the

Li_2MCl_6 (M = Zr, Hf) shows good interfacial stability toward Li-metal, enabling the stable cycling of symmetric cell as long as 4000 h. Finally, we demonstrate a stable prototype ASSLMB by using Li_2MCl_6 (M = Zr, Hf) as a single SE without any surface modifications.

A Li−Zr−Cl Neural Network potential was first trained based on 34 648 configurations (Figure 1a, Table S1) and utilized to determine the thermodynamics of $(LiCl)_{1-x}(ZrCl_4)_x$ phases as shown in Li−Zr−Cl Gibbs triangle diagram (Figure S1). At least 20 000 minima are visited for each composition with up to 52 atoms in the unit cell, where 5052 distinct minima in total with non-$P1$ space group are collected. On the basis of those minima, we plot the thermodynamics convex hull for $(LiCl)_{1-x}(ZrCl_4)_x$ (Figure 1b) and the color bar in the figure illustrates the energy spectrum of distinct minima of each composition. Only the convex point corresponds to Li_2ZrCl_6 (referred to as LZrC hereafter) indicating that LZrC is the only thermostable stoichiometric ratio (Figure S2), whereas the material at other ratios will degenerate into separated LZrC and LiCl or $ZrCl_4$.

SSW-NN global optimization results revealed that the new phase, LZrC, with the structure composed of $LiCl_6^{5-}$ and $ZrCl_6^{2-}$ octahedra sharing common edges and forming layer-by-layer configuration along the c-axis (Figure 1b, Figure S3, and Figure S4, referred to as Ideal/M_defect Layered Structure hereafter) that differs from previously reported
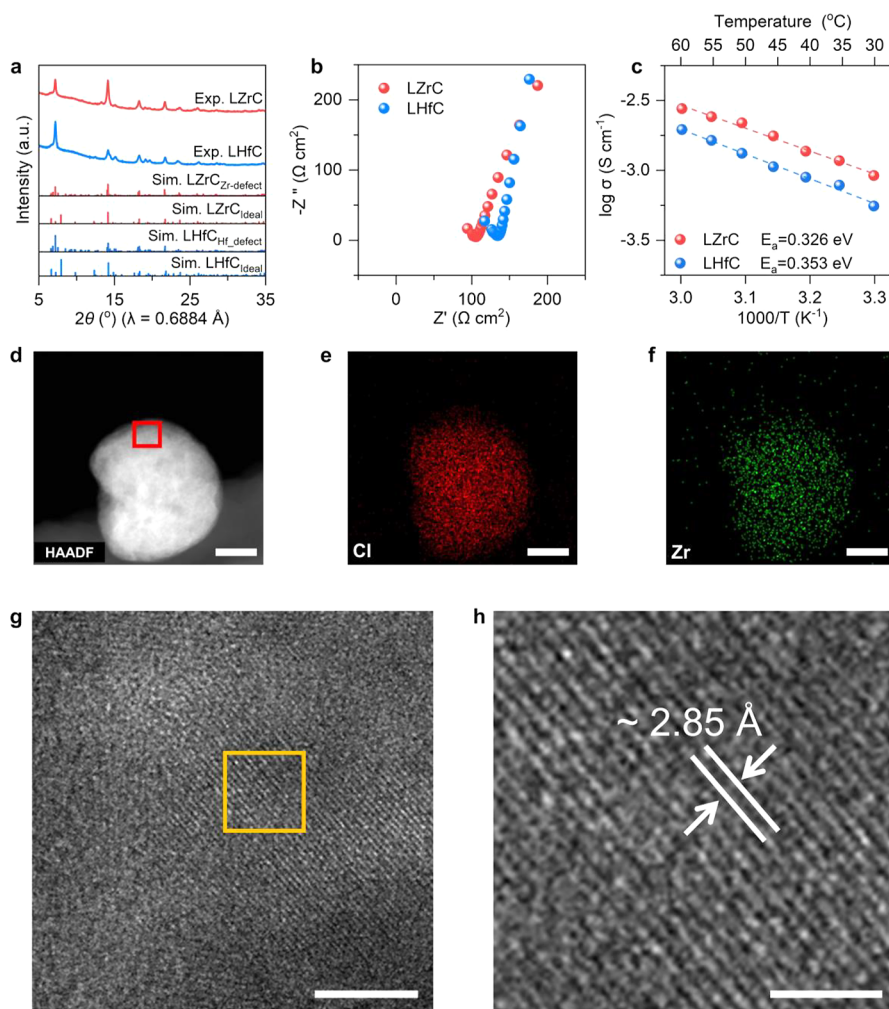
Figure 2. Characterizations of the synthesized layer structured Li_2MCl_6 (M = Zr, Hf) SEs. (a) Synchrotron and simulation X-ray diffraction patterns of the LZrC (red patterns) and LHfC (blue patterns). All of the patterns were indexed to the same space group, $P\bar{3}1c$ and $P2/m$. (b) Nyquist plots of the EIS measurement results of cold-pressed SEs pellets with nonreversible electrodes at 30 °C. The plotted conductivity represents the sum of the grain boundary and bulk conductivities. The thickness of the pellet is around 1 mm. The impedances are normalized to the respective effective contact area. (c) Arrhenius plots of ionic conductivities values of the prepared SEs pellets in the temperature range from 30 to 60 °C for the calculation of migration activation energy. (d−f) HAADF-STEM image and corresponding elemental mapping images of layer structured LZrC, respectively. Scale bar: 50 nm. (g) Corresponding HRTEM image of the selected red box area in (d). Scale bar: 5 nm. (h) Magnified HRTEM image of the selected orange box area in (g). Scale bar: 2 nm.

halide SEs.[18−22] Such a coordination condition for Zr, Li, and Cl are also consistent with Pauling's rules of ion-crystals.[39] However, an important fact is that the difference of potential energy at 0 K between irregular and perfect arrangement of layered structures is about 0.01−0.4 kJ/mol, revealed by SSW NN and first-principles calculations. The almost negligible difference of potential energy leads to the mixed layered structure based on an irregular/perfect arrangement, especially for the actual structure of LZrC obtained by mechanochemical milling. Zr_defect Layered Structure contains two types of layers with adequate intrinsic vacancies based on six-coordinating halogen anion octahedral-sites (Oct-sites) occupied by Zr^{4+} and Li^+ cations (Figure S4). The isostructural layered Li_2HfCl_6 (referred to as LHfC hereafter) can be also obtained due to the analogous physicochemical properties, including charge (Zr^{4+} and Hf^{4+}), ionic radius (r_{Zr} = 72 pm and r_{Hf} = 71 pm),[40] and electronegativity (χ_{Zr} = 1.4 and χ_{Hf} = 1.3).[41]

To investigate the thermodynamic stability of LZrC/Li-metal, we reparametrized the Li−Zr−Cl potential by adding 5784 extra structures to the training set (Table S2). The model of the interface is composed of a four-layer LZrC (001) slab being 20.5 Å thick, and five-layer face-centered cubic (fcc) Li (111) slab being 9.7 Å thick. The fcc Li is the global minimum of Li-metal at 0 K,[42] and the mismatch of lattice parameter between Li (111) and LZrC (001) is only 1.08% (Table S3). A fix lattice local optimization is first performed, where the Li atoms at the interface layer of LZrC are hopping toward the bulk of LZrC, occupying Oct-vacancies between two layers (Figure 1c). For simplicity, the Li^+ being inside the LZrC layer and between two LZrC layers are noted as Li_A and Li_B, respectively. Taking this configuration as the starting point, a 2 ns molecular dynamics (MD) simulation is performed at 300 K. Li_B ions trigger adjacent Li_A ions hopping toward the upper layers (Figure 1d). Zr atoms start to dissolve into Li at 35 ps (Figure 1e), which is determined by the dissolved Zr atoms breaking its last Zr−Cl bond (2.68 Å). After 2 ns, 67% percent
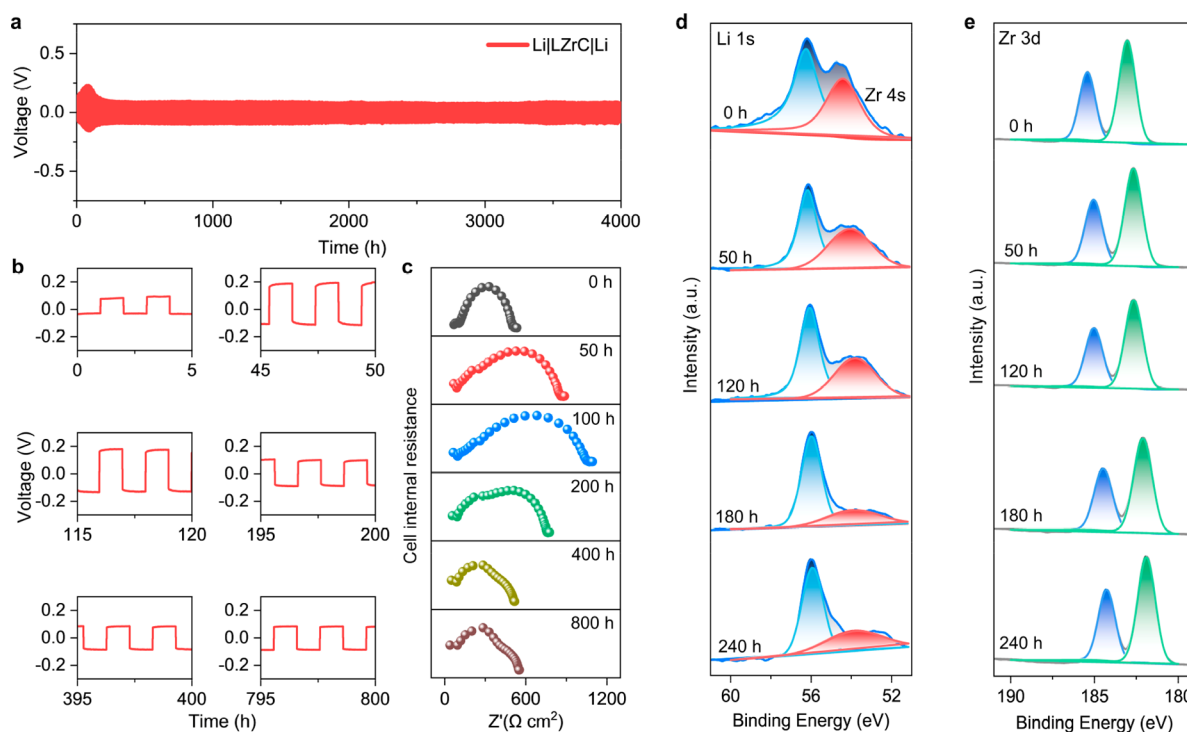
Figure 3. Performance and interface analysis of all-solid-state lithium symmetric cell with layered structure LZrC SE operating at 30 °C. (a) Galvanostatic stripping/plating voltage profiles of a symmetric solid-state Li|LZrC|Li cell during 4000 h (around half a year) cycling. The current density was fixed at 0.1 mA cm^{-2} with a plating/stripping capacity of 0.1 mA h cm^{-2}. (b) Magnified voltage profiles at 0−5, 45−50, 115−120, 195−200, 395−400, and 795−800 h. (c) Nyquist plots of the EIS measurement results of symmetric solid-state cells after 0, 50, 100, 200, 400, and 800 h galvanostatic cycling, respectively. The change of cell internal resistance can be used to explain the evolution process of the interface of Li/LZrC. The impedances are normalized to the respective effective contact area. (d,e) Li 1s, Zr 4s, and Zr 3d XPS spectra of LZrC obtained from symmetric solid-state Li|LZrC|Li cells galvanostatic cycled at 0, 1, 120, 180, and 240 h, respectively. Note that all the ASSLMBs were tested in Coin cells without applying external pressure.

of Zr have dissolved into Li slab. To speed up the interfacial scrutinization, we have also performed a simulation at 400 K for 2 ns and optimized the last snapshot of the trajectory and Li$^+$ probability density from MD simulation (Figure 1f). We can see that all Zr at the interface layer dissolved into a Li slab, leaving a four atomic layer thick LiCl-film between LZrC and the Li slab, preventing further dissolving of Zr. These simulation results indicate the interfacial stability of LZrC/Li-metal.

LZrC and LHfC SEs were synthesized via mechanochemical reactions and confirmed as phase-pure polycrystalline with layered structures revealed by synchrotron radiation X-ray diffraction (SRXRD) patterns (Figure 2a). SRXRD patterns can be indexed well with simulated structure showing representative intensive diffraction peaks. In order to verify the crystal structure of LZrC consisting of defects and metastable nonperiodic features, both the Ideal and M-defect Layered Structure were chosen as models for Rietveld-refinement. The results are shown in Figures S5−S8, and the crystallographic details are summarized in Tables S4−S7, respectively.

The Ideal Layered Structure (Figure S9a, Table S4), consisting of LiCl$_6^{5-}$ and ZrCl$_6^{2-}$ octahedra sharing a common edge, was obtained by refinement matched well with the SSW-NN results (Figure S3). The unit cell of LZrC based on Zr-defect Layered Structure contains two types of layer with adequate intrinsic vacancies (denoted as Layer A and B) based on six-coordinating halogen anions Oct-sites occupied by Zr^{4+} and Li$^+$ cations (Figure S9b). Layer A is Zr-rich while Layer B

is Zr-deficient, both consisting of edge-sharing LiCl$_6^{5-}$ and ZrCl$_6^{2-}$ octahedrons (Li$_{Oct}$−Li$_{Oct}$ and Li$_{Oct}$−Zr$_{Oct}$), and reveal a novel layered structure quietly different from recent reports.[43,44] An important fact is that it is difficult to form edge-sharing ZrCl$_6^{2-}$ octahedrons (Zr$_{Oct}$−Zr$_{Oct}$) due to the strong Coulombic repulsion between Zr^{4+} cations induced by the higher valence state (4+) and smaller ionic radius (72 pm). Furthermore, the potential energy of layered structure based on edge-sharing Zr$_{Oct}$−Zr$_{Oct}$ (Figure S9c) is 8 eV higher than that based on edge-sharing Li$_{Oct}$−Li$_{Oct}$ and Li$_{Oct}$−Zr$_{Oct}$ (Figure S9a,b). Thus, it is impossible for the stable existence of edge-sharing Zr$_{Oct}$−Zr$_{Oct}$ of LZrC in our simulation. This is the latest proposed viewpoint and an important difference: the novel layered LZrC only contains edge-sharing Li$_{Oct}$−Li$_{Oct}$ and Li$_{Oct}$−Zr$_{Oct}$ without edge-sharing Zr$_{Oct}$−Zr$_{Oct}$, both in the Ideal and Zr-defect Layered Structure (Figure S9a,b), compared to the Rietveld-refinement results based on the Li$_3$MCl$_6$ (M = Y/In) crystal (Figure S9d,e). Such refinement shows excellent agreement between the observed and calculated data, indicating that actual LZrC consists of the Ideal and Zr-defect Layered Structure.

To reveal the local chemical environment of lithium in layered SEs, ^{7}Li magic-angle spinning nuclear magnetic resonance (MAS NMR) spectroscopy was performed (Figure S10). One broad peak (10.48, 12.28 ppm for LZrC and LHfC) is observed, which is consistent with the considerable similar Oct-sites of lithium in the predicted structure. In addition, the density of cold-pressed LZrC and LHfC is ∼2.31 and ∼2.75 g cm^{-3} (Table S8), respectively, close to the theoretical density.
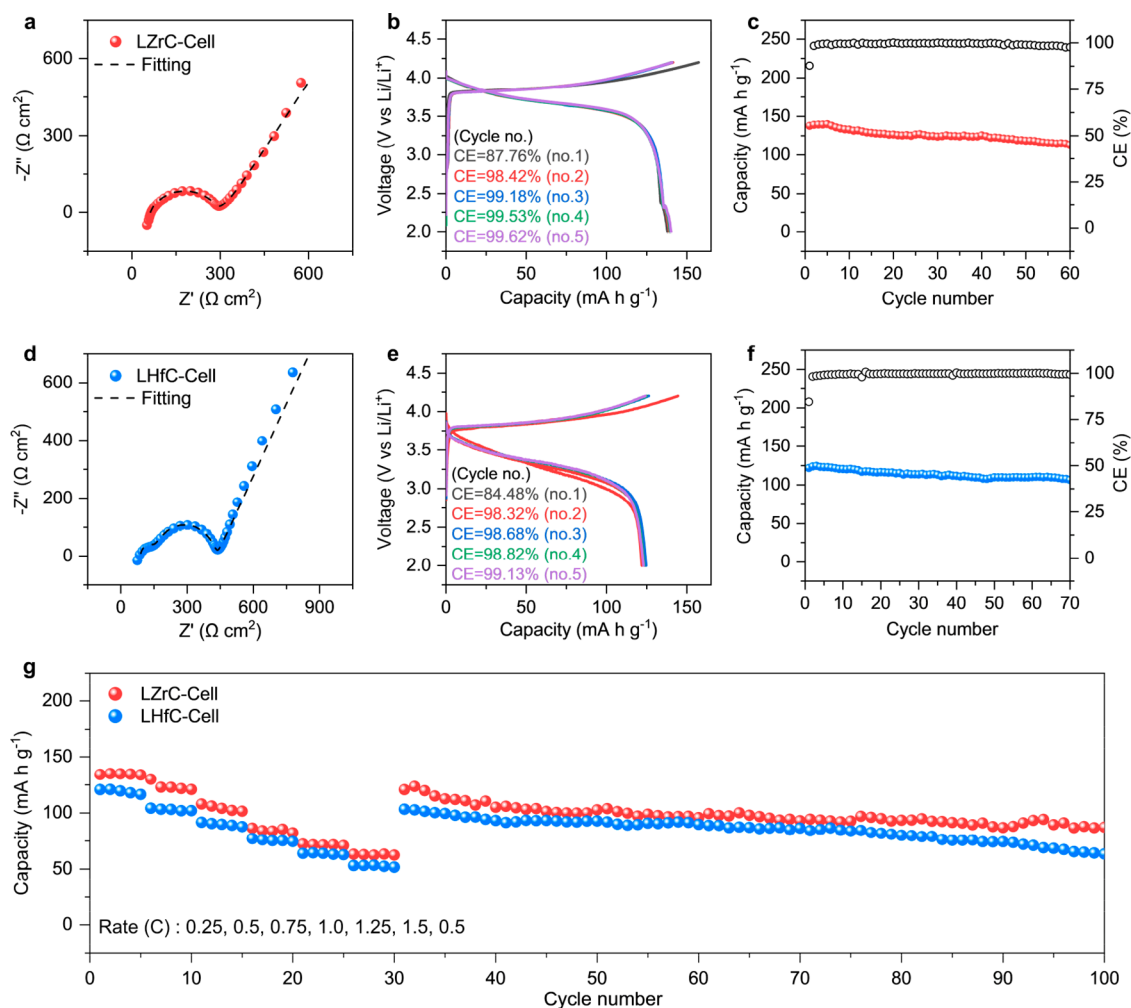
Figure 4. Electrochemical performance of the fabricated ASSLMBs with layer structured Li_2MCl_6 (M = Zr, Hf) SEs and Li metal anodes operating at 30 °C. (a−c) Nyquist plots of the EIS measurement results and fitting profile, corresponding charge/discharge voltage profiles, and capacity and CE as a function of cycle number of Li|LZrC|S-NMC prototype cell cycled at the charge/discharge rate of 0.5/0.25 C, respectively. (d−f) Nyquist plots of the EIS measurement results and fitting profile, corresponding charge/discharge voltage profiles, and capacity and CE as a function of cycle number of Li|LHfC|S-NMC prototype cell cycled at the charge/discharge rate of 0.5/0.25 C, respectively. Solid and hollow circles represent capacity and CE, respectively. The impedances are normalized to the respective effective contact area. (g) Rate capabilities of the Li|Li_2MCl_6 (M = Zr, Hf)|S-NMC cells tested at various C-rates from 0.25 to 1.5 C. All of the ASSLMBs were tested at the voltage window of 2.0−4.2 V vs Li/Li$^+$ in Coin cells without applying external pressure.

The high densification (90.94% for LZrC and 83.28% for LHfC, Table S8) also revealed the excellent deformability, facilitating the fabrication of ASSLMBs without needing high-temperature annealing.

Multiple repeated measurements for ionic conductivity of LZrC and LHfC confirmed the highly reliable superionic conductivity of ∼1.0 and ∼0.5 mS cm^{-1} at 30 °C, respectively (Figure 2b, Table S9). The Li$^+$ migration activation energy (Ea) of LZrC (0.326 eV) and LHfC (0.353 eV) was calculated on the basis of the plots of Arrhenius diagrams (Figure 2c) obtained from Nyquist plots at different temperatures (Figure S11 and Figure S12). Furthermore, transmission electron microscopy (TEM) prepared by solvent-free method was performed to investigate the morphology and crystal lattice of halide SEs. To confirm the incorporation of Cl and Zr into the LZrC particle (Figure 2d), the spatial distributions of Cl and Zr species were revealed by the corresponding elemental mapping (Figure 2e,f), both of which overlapped well with each other, suggesting that Cl and Zr species are mixed well. The typical high-resolution TEM (HRTEM) images (Figure

2g,h) of the selected area in LZrC particle (Figure 2d, red box) revealed a lattice distance of ∼0.285 nm, corresponding to that of crystal plane located at 14.15° (Figure 2a), demonstrating the reliability of halide SEs designed by SSW-NN.

The superionic conductivity, relatively low electronic conductivity (2.66 × 10^{-9} S cm^{-1} for LZrC and 3.69 × 10^{-8} S cm^{-1} for LHfC) (Figure S13), attractive thermodynamic stable interface with Li-metal, and high-abundance of Zr and Hf in Earth's crust (Figure S14) implied enormous promises for SEs for stable ASSLMBs. To show the Li$^+$ migration pathways of layered LZrC, we performed a series of MD simulations at different temperatures (Figure S15 and Table S10). From the mean-square-displacement (MSD) (Figure S16) and the Li$^+$ hopping progress (Movie S1), we have discovered anisotropic three-dimensional (3D) Li$^+$ migration mainly consisting of three channels, that is, hopping perpendicular to the layer (channel$_I$, Li$_A$ to Li$_B$), translate within the interspace between layers (channel$_{II}$, Li$_B$ to Li$_B$), and translate within layer (channel$_{III}$, Li$_A$ to Li$_A$) (Figure S17 and Figure S18), where the barriers fall into a range of 0.14−

0.67 eV. The barriers of channel$_I$ and channel$_{II}$ are lower than that of channel$_{III}$, being close to the Ea (experimental value), representing the mainly migration pathways (further discussion can be found in Note S1).

Symmetric Li−Li cells (Figure S19) without any buffer layers were constructed to verify the interfacial stability of halide SEs/Li-metal. The Li plating/stripping voltage profiles and relevant electrochemical analysis are shown in Figure 3a to c. It is impressive that the Li|LZrC|Li cell cycled for more than 4000 h and exhibited low hysteresis (70 mV) without any sign of short-circuit (Figure 3a), which is the respectable performance among the reported halide and sulfide SEs (Table S11). At an increased capacity of 1.0 mA h cm^{-2} (Figure S20), the stable cycling beyond 1600 h and stable hysteresis (90 mV) can still be attained. The cell comprised of Li|LHfC|Li showed similar performance (Figures S21−S23).

To monitor the interfacial variation of the LZrC/Li, the impedance was measured with an aging time from 0 to 24 h, and the results were analyzed using model fitting[45,46] (Figure S24a,b). With the time increasing, the interfacial area-resistance (R_3) increased within 12 h and then gradually tended to be stable in 24 h (Figure S24c,d), indicating the gradual formation of stable interface during the steady aging state as predicted by MD simulation. For the cycling state, the magnified voltage profiles for cycle time from 0 to 5 h, 45 to 50 h, 115 to 120 h, 195 to 200 h, 395 to 400 h, and 795 to 800 h are provided to show the variation of the voltage plateau (Figure 3b). Correspondingly, the resistance variation is consistent with the evolution of plating/stripping voltage plateau, exhibiting an initial trend of increase and then decrease within 200 h and finally stabilizing within the following cycling process (Figure 3c).

X-ray photoelectron spectroscopy (XPS) and scanning electron microscope (SEM) were conducted to examine the composition and morphology evolution of LZrC. Figure 3d,e compares the high-resolution spectra of Li 1s, Zr 4s, and 3d of cycled-LZrC. All Li 1s spectra only displayed a main peak at ~56.2 eV assigned to Li$^+$ with the absence of the reductive Li. The results coincide with the surface morphology evolutions of cycled Li-metal (Figure S25), indicating the dendrites-free deposition. Both the signal of Zr 4s and 3d spectra exhibited a shift to lower binding energy and a little decrease in the relative intensity of peak at 54.5 eV without any Zr^0 signal,[47] indicating that the surface of LZrC was only slightly reduced under cycling. The atomic ratio analysis of Li, Cl, and Zr of cycled LZrC (Figure S26) confirmed the formation of an Li$^+$-rich interface-layer. In addition, the interfacial variation and relative XPS and SEM analysis of cycled LHfC are similar (Figures S27−S30), indicating the good interfacial stability of layered halide SEs.

ASSLMBs (Figure S31) without high external-pressure consisting of single-crystal LiNi$_{0.5}$Mn$_{0.3}$Co$_{0.2}$O$_2$ (S-NMC) (Figure S32) and layered SE were assembled via cold-pressing. To reveal the internal-resistance of the ASSLMBs, the impedance analysis was conducted. Both Nyquist plots consisted of intercepts, semicircles followed by low-frequency Warburg tail (Figure 4a,d), and the resistance values (Table S12) were fitted based on an equivalent circuit model[18] (Figure S33). The small intercept values in the high-frequency represents the low resistance of the SEs. The semicircles are attributed to the interfacial charge transfer at the S-NMC/SE interface (R_2) and the resistance of Li/SE (R_3), respectively. The charge-transfer resistance of S-NMC/SE is only 19.48 and 57.35 Ω cm^2 for LZrC and LHfC, indicating the excellent interface compatibility enabled by the halide SEs.

Both LZrC-cell and LHfC-cell show good electrochemical performance in terms of initial Coulombic efficiency (referred to as ICE hereafter), cycling stability, and rate capability. LZrC-cell and LHfC-cell exhibited high ICE of 87.76% (Figure 4b) and 84.48% (Figure 4e), respectively, indicating that most of the lithium from the cathode was deposited as metallic lithium during charging without serve side-reactions. Furthermore, the CE was improved up to 99% after fifth cycling, indicating the rapid formation of stable interphase of SEs/electrodes. Stable cycling was achieved in both cells. The LZrC-cell delivered reversible capacity of 113 mA h g^{-1} for 60 cycles with a capacity retention of 82% and an average CE of 99.2% (Figure 4c), and LHfC-cell delivered reversible capacity of 106.5 mA h g^{-1} for 70 cycles with a capacity retention of 87% and an average CE of 99.48% (Figure 4f) at 0.5 C. Furthermore, the capacity retention of ~64% up to 100 cycles at ~2.0 C was achieved in both LZrC-cell and LHfC-cell (Figure S34). It is worth noting that this is the first time to demonstrate the prototype ASSLMBs adopting single SE without any interfacial modifications (Table S13). Moreover, LZrC-cell and LHfC-cell had good rate capabilities. With the charge/discharge rate of 0.25, 0.5, 0.75, 1.0, 1.25, and 1.5 C, the LZrC-cell (LHfC-cell) delivered reversible capacities of 134 (121), 130 (104), 108 (92), 86 (77), 73 (64), and 63 (53) mA h g^{-1}, respectively. After the rate performance test, the capacity can recover to 120 mA h g^{-1} for LZrC-cell and 103 mA h g^{-1} for LHfC-cell at 0.5 C and then continue cycling up to 100 cycles (Figure 4g). The halide SEs were also evaluated by ASSLBs using Li−Sn alloy, exhibiting good rate capabilities and stability (Figures S35−S38 and Note S2).

In summary, we have developed a SSW-NN method to search for stable halide SE on the basis of three primary Li, Zr (Hf), and Cl elements. We have demonstrated that the obtained layer SEs are good for stabilizing ASSLMBs in terms of the superionic conductivity, desirable deformability, and excellent interfacial stability. The superionic conductivity of the cold-pressed pellets reached ~1.0 mS cm^{-1} for LZrC and ~0.5 mS cm^{-1} for LHfC. The fabricated ASSLMBs using layered halide SEs exhibited excellent cycling stability and rate capability due to the stable Li/SE interface (4000 h steady plating/stripping) and low interfacial resistance of S-NMC/SE and P-NCA/SE. Our developed machine learning strategy for LZrC and LHfC SEs will open a new avenue in the development of stable ASSLMBs.

■ ASSOCIATED CONTENT

ⓈⒾ Supporting Information

The Supporting Information is available free of charge at https://pubs.acs.org/doi/10.1021/acs.nanolett.2c00187.

Experimental section for machine learning details, material synthesis, characterization, and measurements (PDF)

CIF files of SSW-NN (ZIP)

Anisotropic three-dimensional (3D) Li ion migration progress in layered structured LZrC (MP4)

■ AUTHOR INFORMATION

Corresponding Authors

Hong-Bin Yao − *Division of Nanomaterials and Chemistry, Hefei National Laboratory for Physical Sciences at the*

Microscale, University of Science and Technology of China, Hefei, Anhui 230026, China; Department of Applied Chemistry, Hefei Science Center of Chinese Academy of Sciences, University of Science and Technology of China, Hefei, Anhui 230026, China; ⊙ orcid.org/0000-0002-2901-0160; Email: yhb@ustc.edu.cn

Cheng Shang − *Collaborative Innovation Center of Chemistry for Energy Material, Shanghai Key Laboratory of Molecular Catalysis and Innovative Materials, Key Laboratory of Computational Physical Science, Department of Chemistry, Fudan University, Shanghai 200433, China; Shanghai Qi Zhi Institute, Shanghai 200030, China;* ⊙ orcid.org/0000-0001-7486-1514; Email: cshang@fudan.edu.cn

Guozhen Zhang − *Division of Nanomaterials and Chemistry, Hefei National Laboratory for Physical Sciences at the Microscale, University of Science and Technology of China, Hefei, Anhui 230026, China;* ⊙ orcid.org/0000-0003-0125-9666; Email: guozhen@ustc.edu.cn

Authors

Feng Li − *Division of Nanomaterials and Chemistry, Hefei National Laboratory for Physical Sciences at the Microscale, University of Science and Technology of China, Hefei, Anhui 230026, China*

Xiaobin Cheng − *Department of Chemical Physics, Hefei Science Center of Chinese Academy of Sciences, University of Science and Technology of China, Hefei, Anhui 230026, China*

Lei-Lei Lu − *Division of Nanomaterials and Chemistry, Hefei National Laboratory for Physical Sciences at the Microscale, University of Science and Technology of China, Hefei, Anhui 230026, China*

Yi-Chen Yin − *Department of Applied Chemistry, Hefei Science Center of Chinese Academy of Sciences, University of Science and Technology of China, Hefei, Anhui 230026, China*

Jin-Da Luo − *Department of Applied Chemistry, Hefei Science Center of Chinese Academy of Sciences, University of Science and Technology of China, Hefei, Anhui 230026, China*

Gongxun Lu − *College of Materials Science and Engineering, Zhejiang University of Technology, Hangzhou, Zhejiang 310014, China*

Yu-Feng Meng − *Division of Nanomaterials and Chemistry, Hefei National Laboratory for Physical Sciences at the Microscale, University of Science and Technology of China, Hefei, Anhui 230026, China;* ⊙ orcid.org/0000-0002-3871-9753

Hongsheng Mo − *Department of Applied Chemistry, Hefei Science Center of Chinese Academy of Sciences, University of Science and Technology of China, Hefei, Anhui 230026, China*

Te Tian − *Division of Nanomaterials and Chemistry, Hefei National Laboratory for Physical Sciences at the Microscale, University of Science and Technology of China, Hefei, Anhui 230026, China*

Jing-Tian Yang − *Department of Applied Chemistry, Hefei Science Center of Chinese Academy of Sciences, University of Science and Technology of China, Hefei, Anhui 230026, China*

Wen Wen − *Shanghai Synchrotron Radiation Facility, Shanghai Advanced Research Institute, Chinese Academy of Sciences, Shanghai 201204, China*

Zhi-Pan Liu − *Collaborative Innovation Center of Chemistry for Energy Material, Shanghai Key Laboratory of Molecular Catalysis and Innovative Materials, Key Laboratory of Computational Physical Science, Department of Chemistry, Fudan University, Shanghai 200433, China; Shanghai Qi Zhi Institute, Shanghai 200030, China;* ⊙ orcid.org/0000-0002-2906-5217

Complete contact information is available at:
https://pubs.acs.org/10.1021/acs.nanolett.2c00187

Author Contributions

◆F.L. and X.C. contributed equally to this work.

Notes
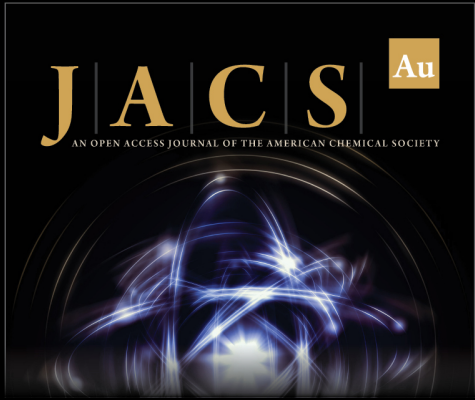
The authors declare no competing financial interest.

■ REFERENCES

(1) Armand, M.; Tarascon, J.-M. Building better batteries. *Nature* **2008**, *451* (7179), 652−657.

(2) Lin, D. C.; Liu, Y. Y.; Cui, Y. Reviving the lithium metal anode for high-energy batteries. *Nat. Nanotechnol.* **2017**, *12* (3), 194.

(3) Chen, R. S.; Li, Q. H.; Yu, X. Q.; Chen, L. Q.; Li, H. Approaching practically accessible solid-state batteries: stability issues related to solid electrolytes and interfaces. *Chem. Rev.* **2020**, *120* (14), 6820−6877.

(4) Famprikis, T.; Canepa, P.; Dawson, J. A.; Islam, M. S.; Masquelier, C. Fundamentals of inorganic solid-state electrolytes for batteries. *Nat. Mater.* **2019**, *18* (12), 1278−1291.

(5) Xiao, Y. H.; Wang, Y.; Bo, S. H.; Kim, J. C.; Miara, L. J.; Ceder, G. Understanding interface stability in solid-state batteries. *Nat. Rev. Mater.* **2020**, *5* (2), 105−126.

(6) Han, X.; Gong, Y.; Fu, K. K.; He, X.; Hitz, G. T.; Dai, J.; Pearse, A.; Liu, B.; Wang, H.; Rubloff, G.; et al. Negating interfacial impedance in garnet-based solid-state Li metal batteries. *Nat. Mater.* **2017**, *16* (5), 572−579.

(7) Huo, H. Y.; Chen, Y.; Li, R. Y.; Zhao, N.; Luo, J.; da Silva, J. G. P.; Mücke, R.; Kaghazchi, P.; Guo, X. X.; Sun, X. L. Design of a mixed conductive garnet/Li interface for dendrite-free solid lithium metal batteries. *Energy Environ. Sci.* **2020**, *13* (1), 127−134.

(8) Wang, C.; Fu, K.; Kammampata, S. P.; McOwen, D. W.; Samson, A. J.; Zhang, L.; Hitz, G. T.; Nolan, A. M.; Wachsman, E. D.; Mo, Y.; et al. Garnet-Type Solid-State Electrolytes: Materials, Interfaces, and Batteries. *Chem. Rev.* **2020**, *120* (10), 4257−4300.

(9) Lee, Y.-G.; Fujiki, S.; Jung, C.; Suzuki, N.; Yashiro, N.; Omoda, R.; Ko, D.-S.; Shiratsuchi, T.; Sugimoto, T.; Ryu, S.; Ku, J. H.; Watanabe, T.; Park, Y.; Aihara, Y.; Im, D.; Han, I. T. High-energy long-cycling all-solid-state lithium metal batteries enabled by silver−carbon composite anodes. *Nat. Energy* **2020**, *5* (4), 299−308.

(10) Kamaya, N.; Homma, K.; Yamakawa, Y.; Hirayama, M.; Kanno, R.; Yonemura, M.; Kamiyama, T.; Kato, Y.; Hama, S.; Kawamoto, K.; Mitsui, A. A lithium superionic conductor. *Nat. Mater.* **2011**, *10* (9), 682−686.

(11) Kato, Y.; Hori, S.; Saito, T.; Suzuki, K.; Hirayama, M.; Mitsui, A.; Yonemura, M.; Iba, H.; Kanno, R. High-power all-solid-state batteries using sulfide superionic conductors. *Nat. Energy* **2016**, *1* (4), 1−7.

(12) Ye, L. H.; Li, X. A dynamic stability design strategy for lithium metal solid state batteries. *Nature* **2021**, *593* (7858), 218−222.

(13) Fu, K.; Gong, Y. H.; Hitz, G. T.; McOwen, D. W.; Li, Y. J.; Xu, S. M.; Wen, Y.; Zhang, L.; Wang, C. W.; Pastel, G.; et al. Three-dimensional bilayer garnet solid electrolyte based high energy density lithium metal-sulfur batteries. *Energy Environ. Sci.* **2017**, *10* (7), 1568−1575.

(14) Wang, R.; Ping, W.; Wang, C.; Liu, Y.; Gao, J.; Dong, Q.; Wang, X.; Mo, Y.; Hu, L. Computation-Guided Synthesis of New Garnet-Type Solid-State Electrolytes via an Ultrafast Sintering Technique. *Adv. Mater.* **2020**, *32* (46), 2005059.

(15) Yang, C.; Xie, H.; Ping, W.; Fu, K.; Liu, B.; Rao, J.; Dai, J.; Wang, C.; Pastel, G.; Hu, L. An electron/ion dual-conductive alloy framework for high-rate and high-capacity solid-state lithium-metal batteries. *Adv. Mater.* **2019**, *31* (3), 1804815.

(16) Banerjee, A.; Wang, X. F.; Fang, C. C.; Wu, E. A.; Meng, Y. S. Interfaces and interphases in all-solid-state batteries with inorganic solid electrolytes. *Chem. Rev.* **2020**, *120* (14), 6878−6933.

(17) Richards, W. D.; Miara, L. J.; Wang, Y.; Kim, J. C.; Ceder, G. Interface stability in solid-state batteries. *Chem. Mater.* **2016**, *28* (1), 266−273.

(18) Asano, T.; Sakai, A.; Ouchi, S.; Sakaida, M.; Miyazaki, A.; Hasegawa, S. Solid Halide Electrolytes with High Lithium-Ion Conductivity for Application in 4 V Class Bulk-Type All-Solid-State Batteries. *Adv. Mater.* **2018**, *30* (44), 1803075.

(19) Schlem, R.; Muy, S.; Prinz, N.; Banik, A.; Shao-Horn, Y.; Zobel, M.; Zeier, W. G. Mechanochemical Synthesis: A Tool to Tune Cation Site Disorder and Ionic Transport Properties of Li_3MCl_6 (M = Y, Er) Superionic Conductors. *Adv. Energy Mater.* **2020**, *10* (6), 1903719.

(20) Li, X. N.; Liang, J. W.; Chen, N.; Luo, J.; Adair, K. R.; Wang, C. H.; Banis, M. N.; Sham, T. K.; Zhang, L.; Zhao, S. Q.; et al. Water-Mediated Synthesis of a Superionic Halide Solid Electrolyte. *Angew. Chem., Int. Ed.* **2019**, *58* (46), 16427−16432.

(21) Li, X.; Liang, J.; Luo, J.; Norouzi Banis, M.; Wang, C.; Li, W.; Deng, S.; Yu, C.; Zhao, F.; Hu, Y.; Sham, T.-K.; Zhang, L.; Zhao, S.; Lu, S.; Huang, H.; Li, R.; Adair, K. R.; Sun, X.; et al. Air-stable Li 3 InCl 6 electrolyte with high voltage compatibility for all-solid-state batteries. *Energy Environ. Sci.* **2019**, *12* (9), 2665−2671.

(22) Liang, J.; Li, X.; Wang, S.; Adair, K. R.; Li, W.; Zhao, Y.; Wang, C.; Hu, Y.; Zhang, L.; Zhao, S.; et al. Site-Occupation-Tuned Superionic Li x ScCl3+ x Halide Solid Electrolytes for All-Solid-State Batteries. *J. Am. Chem. Soc.* **2020**, *142* (15), 7012−7022.

(23) Liang, J. W.; Li, X. N.; Adair, K. R.; Sun, X. L. Metal Halide Superionic Conductors for All-Solid-State Batteries. *Acc. Chem. Res.* **2021**, *54* (4), 1023−1033.

(24) Connell, J. G.; Fuchs, T.; Hartmann, H.; Krauskopf, T.; Zhu, Y. S.; Sann, J.; Garcia-Mendez, R.; Sakamoto, J.; Tepavcevic, S.; Janek, J. r. Kinetic versus Thermodynamic Stability of LLZO in Contact with Lithium Metal. *Chem. Mater.* **2020**, *32* (23), 10207−10215.

(25) Sanchez-Lengeling, B.; Aspuru-Guzik, A. Inverse molecular design using machine learning: Generative models for matter engineering. *Science* **2018**, *361* (6400), 360−365.

(26) Zhao, C.; Wang, Q.; Yao, Z.; Wang, J.; Sanchez-Lengeling, B.; Ding, F.; Qi, X.; Lu, Y.; Bai, X.; Li, B.; Li, H.; Aspuru-Guzik, A.; Huang, X.; Delmas, C.; Wagemaker, M.; Chen, L.; Hu, Y.-S. Rational design of layered oxide materials for sodium-ion batteries. *Science* **2020**, *370* (6517), 708−711.

(27) Bartók, A. P.; De, S.; Poelking, C.; Bernstein, N.; Kermode, J. R.; Csányi, G.; Ceriotti, M. Machine learning unifies the modeling of materials and molecules. *Sci. Adv.* **2017**, *3* (12), No. e1701816.

(28) Shang, C.; Liu, Z. P. Stochastic surface walking method for structure prediction and pathway searching. *J. Chem. Theory. Comput.* **2013**, *9* (3), 1838−1845.

(29) Huang, S. D.; Shang, C.; Zhang, X. J.; Liu, Z. P. Material discovery by combining stochastic surface walking global optimization with a neural network. *Chem. Sci.* **2017**, *8* (9), 6327−6337.

(30) Huang, S. D.; Shang, C.; Kang, P. L.; Zhang, X. J.; Liu, Z. P. LASP: Fast global potential energy surface exploration. *WIREs Comput. Mol. Sci.* **2019**, *9* (6), No. e1415.

(31) Ma, S.; Huang, S. D.; Liu, Z. P. Dynamic coordination of cations and catalytic selectivity on zinc−chromium oxide alloys during syngas conversion. *Nat. Catal.* **2019**, *2* (8), 671−677.

(32) Li, X. T.; Chen, L.; Shang, C.; Liu, Z. P. In Situ Surface Structures of PdAg Catalyst and Their Influence on Acetylene Semihydrogenation Revealed by Machine Learning and Experiment. *J. Am. Chem. Soc.* **2021**, *143* (16), 6281−6292.

(33) Liu, Q. Y.; Shang, C.; Liu, Z. P. In Situ Active Site for CO Activation in Fe-Catalyzed Fischer−Tropsch Synthesis from Machine Learning. *J. Am. Chem. Soc.* **2021**, *143* (29), 11109−11120.

(34) Fang, Y.-H.; Ma, S.-C.; Liu, Z.-P. 3-D Tunnel TiO2 Crystal Phase as a Fast Charging Lithium Battery Anode from Stochastic Surface Walking-Based Material Screening. *J. Phys. Chem. C* **2019**, *123* (32), 19347−19353.

(35) Guan, S.-H.; Shang, C.; Liu, Z.-P. Resolving the temperature and composition dependence of Ion conductivity for yttria-stabilized zirconia from machine learning simulation. *J. Phys. Chem. C* **2020**, *124* (28), 15085−15093.

(36) Steinhardt, P. J.; Nelson, D. R.; Ronchetti, M. Bond-orientational order in liquids and glasses. *Phys. Rev. B* **1983**, *28* (2), 784−805.

(37) Zhang, X. J.; Shang, C.; Liu, Z. P. Pressure-induced silica quartz amorphization studied by iterative stochastic surface walking reaction sampling. *Phys. Chem. Chem. Phys.* **2017**, *19* (6), 4725.

(38) Momma, K.; Izumi, F. VESTA 3 for three-dimensional visualization of crystal, volumetric and morphology data. *J. Appl. Crystallogr.* **2011**, *44* (6), 1272−1276.

(39) Pauling, L. The principles determining the structure of complex ionic crystals. *J. Am. Chem. Soc.* **1929**, *51* (4), 1010−1026.

(40) Shannon, R. D. Revised effective ionic radii and systematic studies of interatomic distances in halides and chalcogenides. *Acta Crystallogr., Sect. A* **1976**, *32* (5), 751−767.

(41) Pauling, L. The nature of the chemical bond. IV. The energy of single bonds and the relative electronegativity of atoms. *J. Am. Chem. Soc.* **1932**, *54* (9), 3570−3582.

(42) Ackland, G. J.; Dunuwille, M.; Martinez-Canales, M.; Loa, I.; Zhang, R.; Sinogeikin, S.; Cai, W. Z.; Deemyad, S. Quantum and isotope effects in lithium metal. *Science* **2017**, *356* (6344), 1254−1259.

(43) Kwak, H.; Han, D.; Lyoo, J.; Park, J.; Jung, S. H.; Han, Y.; Kwon, G.; Kim, H.; Hong, S.-T.; Nam, K.-W.; Jung, Y. S. New Cost-Effective Halide Solid Electrolytes for All-Solid-State Batteries: Mechanochemically Prepared Fe3+-Substituted Li2ZrCl6. *Adv. Energy Mater.* **2021**, *11* (12), 2003190.

(44) Wang, K.; Ren, Q.; Gu, Z.; Duan, C.; Wang, J.; Zhu, F.; Fu, Y.; Hao, J.; Zhu, J.; He, L.; Wang, C.-W.; Lu, Y.; Ma, J.; Ma, C. A cost-effective and humidity-tolerant chloride solid electrolyte for lithium batteries. *Nat. Commun.* **2021**, *12* (1), 1−11.

(45) Riegger, L. M.; Schlem, R.; Sann, J.; Zeier, W. G.; Janek, J. Lithium-Metal Anode Instability of the Superionic Halide Solid Electrolytes and the Implications for Solid-State Batteries. *Angew. Chem., Int. Ed.* **2021**, *60* (12), 6718−6723.

(46) Krauskopf, T.; Hartmann, H.; Zeier, W. G.; Janek, J. r. Toward a fundamental understanding of the lithium metal anode in solid-state batteries—an electrochemo-mechanical study on the garnet-type solid electrolyte Li6. 25Al0. 25La3Zr2O12. *ACS Appl. Mater. Interfaces* **2019**, *11* (15), 14463−14477.

(47) Zhu, Y. S.; Connell, J. G.; Tepavcevic, S.; Zapol, P.; Garcia-Mendez, R.; Taylor, N. J.; Sakamoto, J.; Ingram, B. J.; Curtiss, L. A.; Freeland, J. W. Dopant-dependent stability of garnet solid electrolyte

interfaces with lithium metal. *Adv. Energy Mater.* **2019**, *9* (12), 1803440.